ISSN 1392–1320 MATERIALS SCIENCE (MEDŽIAGOTYRA). Vol. XX, No. X. 2027

Microstructure, Wear and Corrosion Resistances of Atmospheric Plasma, Detonation, High Velocity Oxy-fuel and High Velocity Air-fuel Sprayed WC-10Co-4Cr Cemented Carbide Coatings

Ting XIA [1], Yueming WANG[1] *, Lu XIE [2]

[1] *School of Materials Science and Engineering, Hunan University of Science and Technology, Xiangtan 411201, People's Republic of China;*
[2] *School of Management Engineering, Jiangsu Urban and Rural Construction Vocational College, Changzhou 213147, People's Republic of China*

http://doi.org/10.5755/j02.ms.44363

Received 24 February 2026; accepted 10 April 2026

WC-10Co-4Cr cemented carbide coating has the advantages of superior wear property and corrosion resistance. WC-10Co-4Cr coatings were prepared on 304 stainless steel substrates by different thermal spray technologies including atmospheric plasma spraying (APS), detonation spraying (DS), high velocity oxy-fuel spraying (HVOFS), and high velocity air-fuel spraying (HVAFS), respectively. The microstructure, tribological properties and corrosion resistances of WC-10Co-4Cr coatings were systematically investigated and compared. The results showed that the Vickers hardness of cemented coatings prepared by APS, DS, HVOF, and HVAF, which were all higher than those of 304 stainless steel, were 771.4 HV, 954.2 HV, 1166.2 HV, and 1162.2 HV, respectively. The volume wear rate of 304 stainless steel was about $(36.82\pm0.80)\times10^{-5}$ $mm^3/N\cdot m$. The volume wear rates of APS, DS, HVOF, and HVAF coatings, which were all lower than that of 304 stainless steel, were about $(7.93\pm0.30)\times10^{-5}$, $(1.51\pm0.20)\times10^{-5}$, $(1.17\pm0.10)\times10^{-5}$, and $(1.10\pm0.10)\times10^{-5}$ $mm^3/N\cdot m$, respectively. In addition, the average friction coefficients of 304 stainless steel substrate, APS coating, DS one, HVOF one and HVAF one were about (0.68±0.03), (0.56±0.02), (0.48±0.01), (0.44±0.01) and (0.43±0.01), respectively. Spalling, microcracks perpendicular to the friction direction, and grooves parallel to the friction direction can be found in the wear marks of WC-10Co-4Cr coatings. Abrasive wear and fatigue wear are the main wear mechanisms of the cemented coatings. During the wear test, the carbide particles in DS, HVOF and HVAF coatings gradually became the main body bearing the friction load. Then the wear resistance of the latter three coatings was all superior to that of APS. Moreover, HVOF and HVAF coatings have better wear performances. For corrosion resistance from high to low were HVAF coating, DS one, HVOF one and APS one, respectively. The HVAF coating demonstrated the highest corrosion potential (-0.37±0.01 V_{SCE}), smallest corrosion current density (1.75±0.02 μA/cm²), and largest corrosion resistance (20438.5 Ω) here. The APS coating had the poorest corrosion resistance among these four coatings.

Keywords: different thermal spray technologies, WC-10Co-4Cr coating, wear resistance, corrosion resistance.

1. INTRODUCTION

WC-10Co-4Cr cemented carbide coating has obvious advantages including wear resistance, fatigue resistance, high temperature resistance, corrosion resistance and so on. It can be widely used as a protective coating on the surface of aircraft landing gear, hydraulic cylinder, valve, water pump mold and so on [1]. WC-10Co-4Cr cemented carbide coatings are usually prepared by atmospheric plasma spraying (APS), detonation spraying (DS), high velocity oxy-fuel spraying (HVOFS) and high velocity air-fuel spraying (HVAFS). APS, which possesses some advantages including high temperature, high energy and high efficiency, is one of the most commonly used coating preparation technologies currently [2]. HVOF, which is widely used to prepare dense coatings with high interlayer bonding strength, has special characteristics including low-temperature and high-speed flame flow [3]. HVAF technology can effectively reduce the degree of oxidation and decarburization of WC coatings during the spraying process due to its relatively low temperature and high spraying speed [4]. DS technology utilizes the enormous energy generated by oxygen and gas ignition explosions to heat and accelerate particles. And then coatings prepared by DS have high density and bonding strength owing to extremely high flight speed and sufficient melting degree of feedstock during spraying [5]. WC-10Co-4Cr coating was prepared on the surface of stainless-steel friction pairs using APS technology by Yuan et al. [6]. Phase structure, corrosion friction characteristics, and electrochemical characteristics of the ceramic coating were investigated. As reported by Yuan et al. [7], two types (nanoscale and microscale) of grain size WC-10Co-4Cr coatings were prepared by APS from nano-aggregated powder and micro-aggregated one. And the influences of grain size on the microstructure and friction properties of APS coatings were systematically analyzed. WC-10Co-4Cr protective coating was prepared on the surface of 304 stainless steel substrate by using HVOF as reported in the work of Huang et al. [8]. And they found out that good friction and corrosion performances of the HVOF coatings were attributed to the synergistic effects between the WC phase for bearing load and the metal bonding phase for producing passivation. Yang et al. [9] prepared WC10Co4Cr coatings

*Corresponding author: Y. Wang
E-mail address: *1030102@hnust.edu.cn*

using hydrogen fuel and kerosene liquid fuel HVOF spraying equipment under 9 different process conditions. The effect of fuel type on the microstructure, residual stress, and mechanical properties of HVOF coatings were investigated in their work. And they found that the friction and wear resistance of HVOF WC-10Co-4Cr coating was superior to that of $Cr_{12}MoV$ cold working die steel. Murthy et al. [10] prepared WC-10Co-4Cr coatings and Cr_3C_2-20(NiCr) coatings by HVOF and DS, respectively. The wear resistance of DS coatings was slightly better than that of HVOF ones due to the higher residual compressive stress of the former. Moreover, the wear resistance of WC-10Co-4Cr coating was higher than that of Cr_3C_2-20(NiCr) one. In another work of Murthy et al. [11], WC-10Co-4Cr coatings were prepared by using HVOF and DS, respectively. And they found that density, microhardness, and residual compressive stress of DS coatings were all higher than those of HVOF ones. As a result, the corrosion resistance of DS coatings was better than that of HVOF ones. Thakare et al. [12] reported the synergistic effect between wear and corrosion of DS WC-10Co-4Cr coatings in alkaline environments. As reported by Samodurovaet al. [13], a WC-10Co-4Cr coating with submicron carbide grains and a porosity of less than 0.5 % was prepared on the surface of Al-Cu-Mg alloy by using DS. WC-10Co-4Cr coatings were prepared on 304 stainless steel from three different particle size raw materials by using HVAF in the work of Huang et al. [14]. And they found out that the erosion wears of the coatings were mainly caused by micro cutting and fatigue peeling at 30° and 90° erosion angles, respectively. As reported by Chen et al. [15], WC-10Co-4Cr coatings were prepared by using HVOF and HVAF techniques, respectively. And they found that the rolling force of next-generation lithium battery rollers can be improved by HVAF coatings as their microhardness, bonding strength and wear resistance were all higher than those of HVOF ones. Wu et al. [16] found that the comprehensive performance of WC-10Co-4Cr coatings prepared by HVOF and supersonic plasma spraying (SPS) were similar. WC-10Co-4Cr coatings exhibited mainly abrasive wear after wear test at 560 r/min for 10 hours, while mainly abrasive wear and contact fatigue occurred after wear test at 1120 r/min for 10 hours. Picas et al. [17] reported that in-flight particle characteristics had a significant effect on the porosity, hardness and corrosion resistance. The highest corrosion resistance was obtained with those parameters that allowed a sufficient melting of the agglomerates while minimizing the decarburization of the WC particles. Recently, ultrasonic vibration-assisted cored wire arc additive manufacturing has been used to improve microstructure and wear performance of WC-reinforced 316L composite coatings [18]. Laser shock peening was used to optimize the microstructure and surface integrity of ceramic-reinforced metal-matrix composite coatings [19]. The particle floating and transfer behavior during cored wire arc additive manufacturing provided valuable insight into the evolution of reinforcement distribution and defect formation [20].

However, there are few reports on comparative analysis of the microstructures, tribological properties, and corrosion performances of WC-10Co-4Cr coatings prepared by different thermal spraying technologies. As a result, WC-10Co-4Cr coatings were prepared on 304 stainless steels by using APS, DS, HVOF, and HVAF, respectively. The microstructures, phase constitutions, wear behavior, and corrosion resistance of these four coatings were systematically analyzed and compared.

2. EXPERIMENTAL PROCESS

2.1. Coating preparation methods

The particle size, flow rate, apparent density, specific heat capacity, and thermal conductivity of WC-10Co-4Cr powder (Praxair Surface Technology Co. Ltd., USA) were (18~45) μm, 12.8 ($s \cdot 50g^{-1}$), 5.7 ($g \cdot cm^{-3}$), 502 ($J \cdot kg^{-1} \cdot K^{-1}$), 75 ($W \cdot m^{-1} \cdot K^{-1}$), respectively. WC-10Co-4Cr powder was treated in a drying oven at 100 ℃ for 30 min to improve flowability. The surface of 304 stainless steel substrates (with a size of 140 × 30 × 6 mm) was cleaned by acetone first, and then they were grit blasted by 120# Al_2O_3 particles (with sandblasting parameters of 0.4 MPa pressure and 80 – 100 mm distance) to get a coarse and fresh surface.

An APS machine (DH-1080, Shanghai Dahao spraying machinery equipment Co., Ltd., China) was selected to prepare NiCrAlY bond coat and ceramic top coat. The APS parameters, including spray power, spray distance, powder feed rate, Ar gas flow rate and H_2 gas flow rate for preparing NiCrAlY bond coat were 26 kW, 120 mm, 0.167 ($dm^3 \cdot s^{-1}$) and 0.0222 ($dm^3 \cdot s^{-1}$), respectively. Those parameters for preparing WC-10Co-4Cr top coat were 33 kW, 120 mm, 0.833 $g \cdot s^{-1}$, 0.222 $dm^3 \cdot s^{-1}$ and 0.0278 $dm^3 \cdot s^{-1}$, respectively.

A DS machine (Dnieper-3, National Academy of Science, Ukraine) was selected to prepare WC-10Co-4Cr top coat and NiCrAlY board one. The DS parameters, including oxygen flow rate, acetylene flow rate, working frequency, powder feed rate, spray angle and spray distance, were 0.417 $dm^3 \cdot s^{-1}$, 0.278 $dm^3 \cdot s^{-1}$, 4 s^{-1}, 1.33 $g \cdot s^{-1}$, 90° and 170 mm, respectively.

The parameters including oxygen flow rate, kerosene flow rate, combustion pressure, powder feed rate, carrier gas flow rate, spray distance and gun moving speed for preparing WC-10Co-4Cr coating using a HVOFS machine (JST5000, Suzhou Jishengte Machinery Equipment Co., Ltd., China) were 0.417 $dm^3 \cdot s^{-1}$, 0.250 $dm^3 \cdot s^{-1}$, 0.65 MPa, 2.00 $g \cdot s^{-1}$, 0.0833 $dm^3 \cdot s^{-1}$, 350 mm and 500 $mm \cdot s^{-1}$, respectively.

WC-10Co-4Cr coating was prepared by a HVAFS machine (M_2h, Unique Coat, USA). The system is equipped with an M_3TM spray gun, with air, propane and N_2 as combustion aid, fuel, and carrier gas, respectively. The HVAF parameters including air pressure, propane pressure, powder feed rate, carrier gas flow rate, spray angle, and spray distance were 1.08 MPa, 1.14 MPa, 2.00 $g \cdot s^{-1}$, 0.0167 $dm^3 \cdot s^{-1}$, 90°, and 360 mm, respectively.

2.2. Friction and wear test

The microhardness was measured using a Vickers hardness tester (Buehler 5410, Buehler Ltd., USA) with a load of 100 g (0.98 N) and a loading time of 15 seconds. The average value was taken from the hardness data measured from 5 points. The friction experiments of WC-

10Co-4Cr coating were investigated on a ball-on-disk high-temperature friction and wear tester (GF-I, Lanzhou Zhongke Kaihua Technology Development Co., Ltd., China) in accordance with ASTM D6279-2003(2013). Friction parameters including load, speed, dwell time, and sliding distance were 60 N, 10 $r \cdot s^{-1}$, 30 min and 5 mm, respectively. Si_3N_4 balls with a diameter of 6 mm were selected as the counterbodies here. The friction coefficient was recorded by a computer during the wear test. Moreover, the reported friction coefficient was the arithmetic mean value from three experiments under same conditions. Cross-sectional morphologies of the wear marks were analyzed, and the wear volume loss of thermal sprayed coatings was calculated by a material surface wear mark measuring instrument (MT-500, Lanzhou Zhongke Kaihua Technology Development Co., Ltd., China). The running distance of the probe was 3 mm. The wear volume loss was then calculated from the measured cross-sectional area of the wear track and the sliding trajectory. Finally, the specific wear rate was obtained by dividing the wear volume by the applied load and the total sliding distance.

2.3. Electrochemical corrosion test

The electrochemical corrosion behaviors of the WC-10Co-4Cr coatings and 304 stainless steel at room temperature were investigated by the polarization method in 3.5 mass % NaCl solution using an electrochemical workstation (CHI660E, Shanghai Chenhua Instrument Co., Ltd., China). The specimens were polished to a mirror surface, and sealed by epoxy resin to expose an area of 1 cm × 1 cm for the corrosion test. During the corrosion test, a conventional three-electrode cell was used, with a coating sample, saturated calomel electrode (SCE), and platinum foil as working, reference, and auxiliary electrode, respectively. The potential was scanned at a sweep rate of 1 $mV \cdot s^{-1}$ from -700 to 1500 mV relative to open-circuit potential (OCP). The electrochemical test was repeated three times to ensure the accuracy of data.

2.4. Microstructure and phase analysis

Particle size distribution of WC-10Co-4Cr powder was measured by a laser particle size analyzer (LA-950, Horiba Ltd., Japan). The morphologies of feedstock, thermal sprayed coatings, wear debris, worn surfaces of coatings and Si_3N_4 ceramic balls, electrochemical corrosion surfaces of WC-10Co-4Cr coatings and 304 stainless steels were characterized by a scanning electron microscope (TescanMira4, Tescan Orsay Holding, Czech Republic). An energy dispersive spectrometer (AztecLiveOneXplore 30, Oxford, UK) was used to measure the element map distribution of a cross-section of a single powder. The phase constituents of WC-10Co-4Cr powder and thermal sprayed coating were analyzed by the X-ray diffractometer (Bruker D8 Advance, Bruker, Germany) with Cu Kα ray (λ = 1.54056 Å). The voltage, current, scanning speed, scanning range and step size were 40 kV, 40 mA, 2(°·min^{-1}), 0°–100° and 0.02°, respectively.

3. RESULTS AND DISCUSSION

3.1. Microstructural characterization

Most of WC-10Co-4Cr powders are spherical as shown in Fig. 1 a. White and dark gray phases are observed in the cross-section of a single powder particle, which is agglomerated from numerous fine primary particles, as shown in Fig. 1 b. It can be seen that W is mainly distributed in the white area (see Fig. 1 c), while Co and Cr are mainly distributed in the dark gray area (see Fig. 1 d and Fig. 1 e). It can be concluded that the white area is mainly composed of WC ceramic phase, while Co-Cr bonding phase is mainly distributed in the dark gray area. In addition, the average particle size of WC-10Co-4Cr powder is 30 μm. And the main particle size distribution of feedstock is ranging from 18 to 45 μm, which is suitable for APS, DS, HVOF, and HVAF.

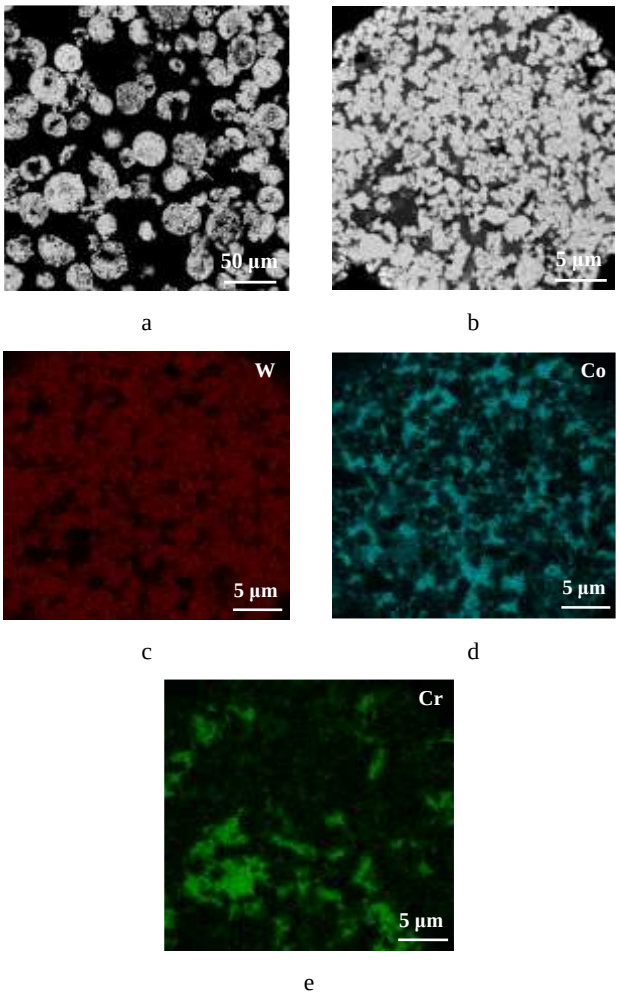

Fig.1. Cross-section of WC-10Co-4Cr powder: a – panorama; b – high magnification image of single powder particle; c – W; d – Co; e – Cr distribution map

The thicknesses of the NiCrAlY bond coat and WC-10Co-4Cr top coat prepared by APS (see Fig. 2 a) are (90 ± 10) μm and (265 ± 10) μm, respectively. A typical lamellar structure of thermal sprayed coating can be found both in bond coat (see Fig. 2 b) and top one (see Fig. 2 c).

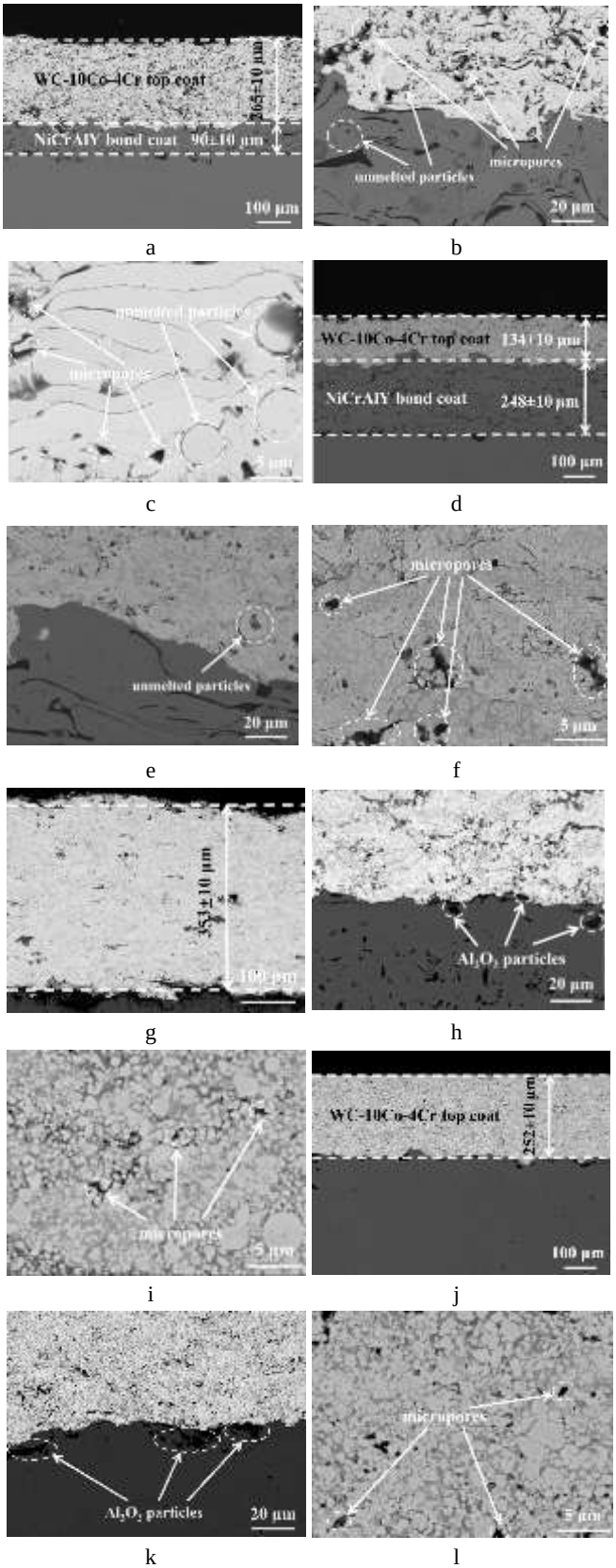

Fig. 2. Cross-section images of WC-10Co-4Cr coating: a – panorama of APS coating; b – image from APS interface region; c – image from APS local region of top surface; d – panorama of DS coating; e – image from DS interface region; f – image from DS local region of top surface, g – panorama of HVOFS coating; h – image from HVOFS interface region; i – image from HVOFS local region of top surface; j – panorama of HVAFS coating; k – image from HVAFS interface region; l – image from HVAFS local region of top surface

The interface between the top layer and transition layer is obviously characterized by mechanical bonding, and some unmelted particles and micropores can be observed in the top coat. As shown in Fig. 2 d, the thickness of APS NiCrAlY bond coat and DS WC-10Co-4Cr top coat are (248 ± 10) μm and (134 ± 10) μm, respectively. Dense and mechanical bonding of the interface between topcoat and bond one can be found as shown in local magnification area (see Fig. 2 e). It should be noted that the particle structure of the original feedstock and many micropores retain in the DS top coating as shown in Fig. 2 f. The thickness of HVOF WC-10Co-4Cr coating without bond coating is (353 ± 10) μm as shown in Fig. 2 g. Dark Al_2O_3 particles, embedded into the surface of the substrate during sand blasting, can be observed in the 304 stainless steel near the bonding interface (see Fig. 2 h). Dense and granular structures with a few micropores are shown in HVOF coatings (see Fig. 2 i). The microstructure of HVAF hard alloy coating is similar to that of HVOF one as shown in Fig. 2 j, k, and l. The thickness of HVAF WC-10Co-4Cr coating without bond coating is (252 ± 10) μm as shown in Fig. 2 j. Dark phase of Al_2O_3 powders were inserted in the surface of 304 stainless steel (see Fig. 2 k), and dense granular structure with a few micropores was formed in HVAF coatings (see Fig. 2 l). A large amount of WC-10Co-4Cr powders were fully melted during high temperature plasma spraying. And then these powders spread and deformed into a clear layered structure after high-speed collision with the matrix or transition layer. Deposition temperatures DS, HVOF and HVAF are relatively low compared to APS. The granular structure of initial feedstock was well preserved in DS, HVOF and HVAF coatings. It is worth noting that the hardness and tribological performances of DS, HVOF, and HVAF coatings will be improved due to the high retention of the WC hard phase in these three samples.

3.2. Phase constitution analysis

XRD patterns of WC-10Co-4Cr powder and coatings prepared by different thermal spray technologies are shown in Fig. 3. The XRD pattern of the original WC-10Co-4Cr powder exhibits prominent diffraction peaks corresponding to the WC phase, accompanied by weak peaks of the W_2C, Co_3W_3C, and Co-Cr bonding phases. The APS coating was dominated by the W_2C phase, indicating severe decomposition and decarburization of WC during spraying. Owing to the extremely high particle temperature in the APS process, WC particles are more likely to undergo thermal decomposition and oxidation-assisted decarburization during flight and deposition, resulting in the formation of W_2C. Similar phase evolution has also been reported by Yuan et al. [21].

Several formation mechanisms of the W_2C phase in thermal sprayed coatings, such as thermal decomposition of WC to generate W_2C and loss of carbon caused by the solid reaction of WC with oxygen, have been proposed by Guilemany et al. [22]. In addition, the dissolution of WC particles in the Co-Cr-based binder during APS and DS was a potential additional mechanism for W_2C formation. Both oxidation decarburization of WC-10Co-4Cr coating and thermal decomposition degree of WC increased with

particle temperature during thermal spraying [23, 24]. It should be noted that almost no differences in phase constituents can be found between XRD peaks of HVOF and HVAF coatings with that of the initial powder. A little possibility of hard phase decomposition and generation of new phases existed during HVOF and HVAF spraying due to no significant melting of powder in low temperature flame. The formation of HVOF and HVAF dense coatings mainly relied on high kinetic energy impact, plastic deformation, flattening, and rapid consolidation of semi-molten or partially softened particles. Additionally, Co_3W_3C phase can be found in XRD patterns of initial powder, DS, HVOF and HVAF coatings (see Fig. 3). Due to its high hardness and brittleness, Co_3W_3C phase can work synergistically with WC one to enhance the wear resistance of WC-10Co-4Cr coating.

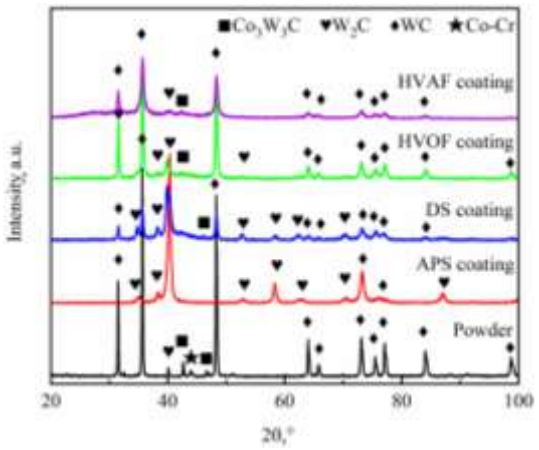

Fig. 3. XRD patterns of WC-10Co-4Cr powder and coatings prepared by thermal spraying

Rapid decarburization of WC occurred owing to the highest temperature of APS among these four thermal spray technologies. The diffraction peaks of APS coating were dominated by the W_2C phase. The diffraction peaks of the DS coating were dominated by W_2C and WC phases due to a certain proportion of decomposition of WC during fabrication. The decomposition degree of the WC phase from high to low was APS, DS, HVOF, and HVAF sequentially.

3.3. Tribological properties of these four coatings

The average values of Vickers hardness of WC-10Co-4Cr coatings from high to low are prepared by HVOF (1166.2 HV), HVAF (1162.2 HV), DS (954.2 HV) and APS (771.4 HV) are shown in Table 1. The lower hardness of APS coating was caused by formation of many micropores and unmelted particles along with massive decomposition of WC phase during atmospheric plasma spraying. Vickers hardnesses of HVOF and HVAF coatings were significantly higher than those of APS and DS ones owing to most of the WC hard phases of feedstock being retained in the first two coatings. Decomposition of a portion of WC hard phase occurred during detonation spraying, and as a result, the hardness of the DS coating was between those of the APS coating and HVOF, HVAF ones. The average friction coefficient and volumetric wear rate of 304 stainless steel substrate and WC-10Co-4Cr coating can be found as shown in Fig. 4.

Table 1. Vickers hardness of WC-10Co-4Cr coating

Sample	Point 1	Point 2	Point 3	Point 4
APS coating	767.9	788.2	773.9	793.0
DS coating	930.8	912.1	944.5	984.7
HVOF coating	1157.1	1169.3	1174.4	1169.0
HVAF coating	1166.8	1146.5	1186.9	1125.7
substrate	317.4	316.7	319.8	300.8

Wear rate of 304 stainless steel is approximately $(36.82\pm0.80)\times10^{-5}$ $mm^3/N\cdot m$. The volume wear rates of APS, DS, HVOF, and HVAF coatings, which are much lower than that of 304 stainless steel, are about $(7.93\pm0.30)\times10^{-5}$, $(1.51\pm0.20)\times10^{-5}$, $(1.17\pm0.10)\times10^{-5}$ and $(1.10\pm0.10)\times10^{-5}$ $mm^3/N\cdot m$, respectively. The average friction coefficients of 304 stainless steel, APS coating, DS coating, HVOF coating and HVAF coating,decreased in the order listed, being (0.68±0.03), (0.56±0.02), (0.48±0.01), (0.44±0.01) and (0.43±0.01), respectively. As reported by Hou et al. [24], the wear resistance of thermal sprayed WC coatings was not only related to their hardness, but also closely related to their fracture toughness and interlayer cohesion. The hardness of APS coating was much lower than those of DS, HVOF and HVAF coatings. Additionally, the APS coating was characterized by low density and weak interlayer cohesion, both of which were directly attributed to the abundant micropores, and cracks present at the interlayer bonding interface. As a result, wear resistance of APS coating was the lowest among these four types of thermal sprayed coatings. On the contrary, the wear resistance of HVOF coating and HVAF coating is relatively superior.

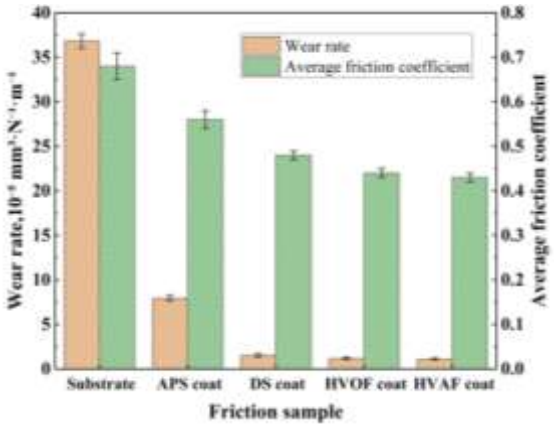

Fig. 4. Average friction coefficient and wear rate of WC-10Co-4Cr coatings and 304 stainless steel substrate

The width of the wear profile of APS coating after wear test for 30 minutes is approximately 1521.4 μm, as shown in Fig. 5 a. Microcracks perpendicular to the movement direction of the counterbody can be found in local magnified images, as shown in Fig. 5 b and c, respectively. The width of the wear profile of the DS coating is about 1349.7 μm, as shown in Fig. 5 d. Microcracks, spalling and grooves can be found in local magnified images of the worn surface of the DS coating, as shown in Fig. 5 e and f, respectively. The width of the wear profile of the HVOF coating is around 1286.9 μm, as shown in Fig. 5 g. Spalling and grooves can be found in local magnified images of the worn surface of HVOF coating, as shown in Fig. 5 h and i, respectively.

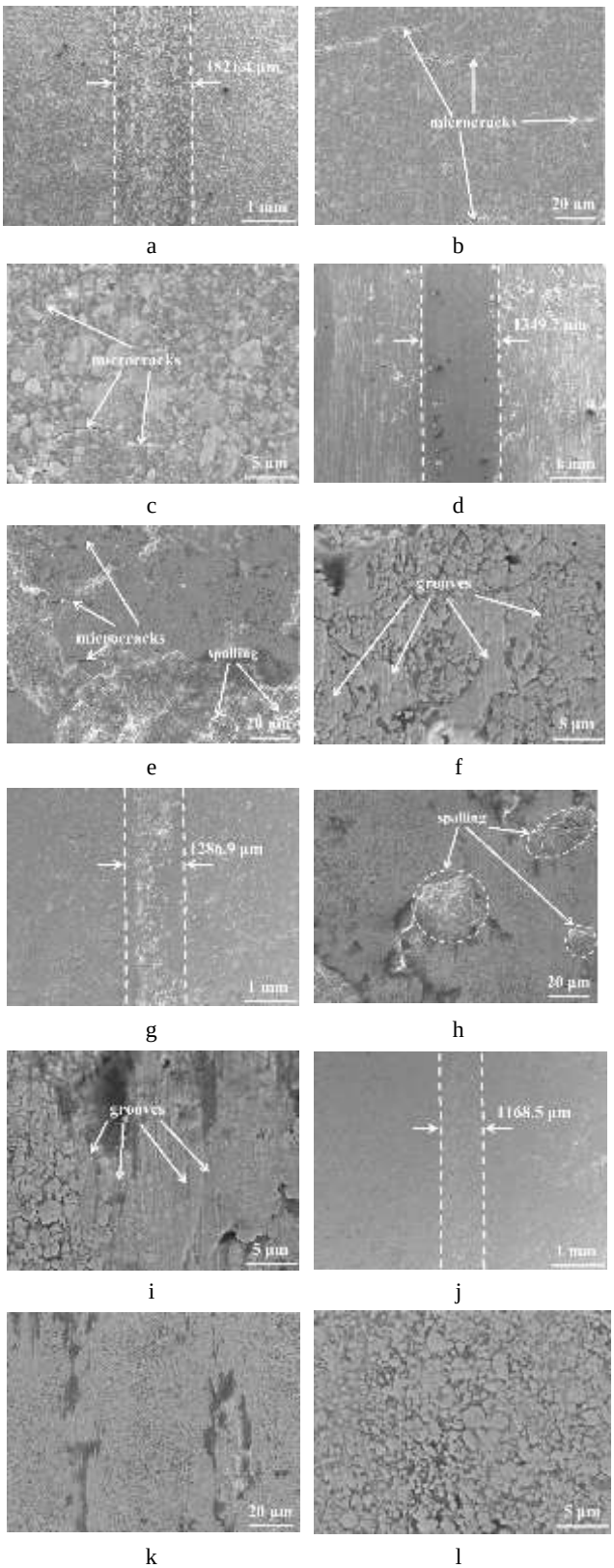

Fig. 5. SEM morphologies of worn surfaces of WC-10Co-4Cr coating after wear test for 30 min: a – panorama; b, c – high magnification images of APS coating; d – panorama; e, f – high magnification images of DS coating; g – panorama; h, i – high magnification images of HVOF coating; j – panorama; k, l – high magnification images of HVAF coating

The width of wear marks on the HVAF coating in Fig. 5 j is approximately 1168.5 μm. Moreover, the worn surface of the HVAF coating is relatively smooth. No obvious spalling and grooves can be found in local magnification areas, both in Fig. 5 k and l. Wear morphologies indicated that abrasive wear and fatigue wear the main wear mechanisms of WC-10Co-4Cr coatings owing to the carbide ceramic hard phase in these thermal-sprayed coatings. In addition, the relatively soft Co–Cr binder phase was preferentially removed during sliding. And then the hard phase of carbide particles in DS, HVOF and HVAF coatings gradually became the main body that bears frictional loads during the reciprocating motion of Si_3N_4 counterbodies. As a result, the wear rate of WC-10Co-4Cr coatings can be effectively reduced.

A wear mark with a diameter of approximately 1575.9 μm was formed on the surface of Si_3N_4 dual counterbodies (see Fig. 6 a) after the friction test on APS coating at room temperature for 30 min.

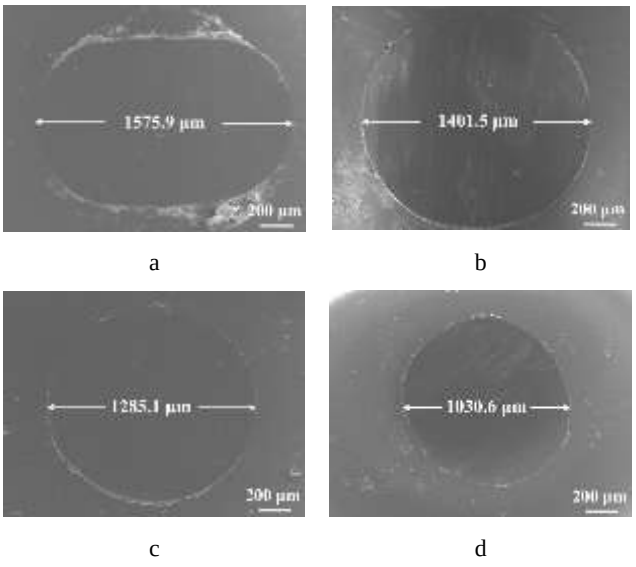

Fig. 6. SEM images of wear scars of Si_3N_4 balls after wear test by WC-10Co-4Cr coatings prepared by: a – APS; b – DS; c – HVOF; d – HVAF

After friction test on DS, HVOF and HVAF coatings for 30 min, the diameter of wear marks on Si_3N_4 counterbodies (see Fig. 6 b, c and d decreased to 1401.5, 1285.1 and 1030.6 μm, respectively. It should be noted that the variation trend of the diameter of wear marks on the surface of Si_3N_4 counterbodies was consistent with that of the width of wear marks on thermal sprayed coatings (see Fig. 5).

Most of the wear debris collected from APS, DS, HVOF and HVAF coatings after wear test at room temperature for 30 min are fine particles with fewer flake-like ones, as shown in Fig. 7. Due to the brittleness of the cemented carbide itself, the wear mechanisms of coatings are mainly abrasive wear and fatigue wear. A large amount of fine particle debris formed owing to friction films on the worn surfaces of WC-10Co-4Cr coatings were prone to cracking and spalling during wear test.

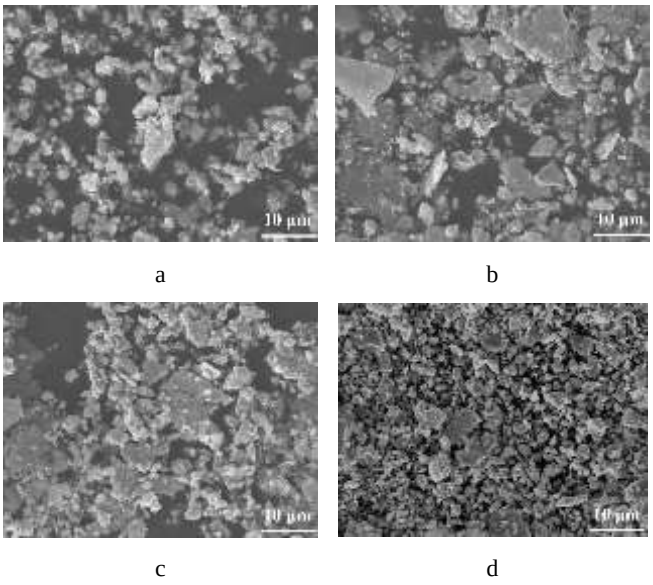

a b

c d

Fig. 7. SEM images (SE) of wear debris collected from WC-10Co-4Cr coatings prepared by: a – APS; b – DS; c – HVOF; d – HVAF

3.4. Corrosion properties of these four coatings

The potentiodynamic polarization curves of WC-10Co-4Cr coatings fabricated by different thermal spray technologies in a 3.5 wt.% NaCl solution are shown in Fig. 8. And corresponding electrochemical parameters, including corrosion potential (E_{corr}), corrosion current density (I_{corr}), corrosion resistance (R) are summarized in Table 2.

Table 2. The electrochemical parameters estimated from polarization data for the WC-10Co-4Cr coatings in 3.5 wt.% NaCl

Sample	Ba, V per decade	Bc, V per decade	E_{corr}, V_{SCE}	I_{corr}, μA/cm²	R, Ω
APS coating	3.631	6.310	-0.50±0.02	19.9±0.06	1367.7
DS coating	4.894	5.778	-0.52±0.02	3.12±0.03	13051.3
HVAF coating	6.051	6.106	-0.37±0.01	1.75±0.02	20438.5
HVOF coating	4.429	5.242	-0.34±0.01	7.74±0.04	5810.9

I_{corr} is a key indicator of corrosion rate, smaller values correspond to lower rates. R reflects the coating's barrier to corrosive media, with higher values signifying stronger protection. The values of E_{corr} and I_{corr} were obtained by fitting the polarization curves using electrochemical analysis software. Therefore, slight visual differences in the curves can't directly reflect the actual values of the fitted electrochemical parameters. The APS coating exhibited the poorest corrosion resistance, with the lowest E_{corr} (-0.50±0.02 V_{SCE}), the highest I_{corr} (19.97±0.06 μA/cm²) and minimal R (1367.7 Ω) as shown in Table 2. Compared to APS coating, the DS one exhibited better corrosion resistance with similar E_{corr} (-0.52±0.02 V_{SCE}), lower I_{corr} (3.12±0.03 μA/cm²) and higher R (13051.3Ω). Compared to DS coating, the HVOF coating has a higher I_{corr} of (7.74±0.04) μA/cm² and a lower R of 5810.9 Ω. And then the corrosion resistance of the HVOF coating was slightly inferior to that of the DS one. The HVAF coating delivered the best electrochemical corrosion performance with the highest E_{corr} (-0.37±0.01 V_{SCE}) and R (20438.5 Ω), the lowest I_{corr} (1.75±0.02 μA/cm²). In terms of corrosion resistance, the four coatings ranked from high to low were HVAF coating, DS one, HVOF one and APS one, respectively. And the corrosion resistances of these four coatings were closely related to their microstructures and phase compositions.

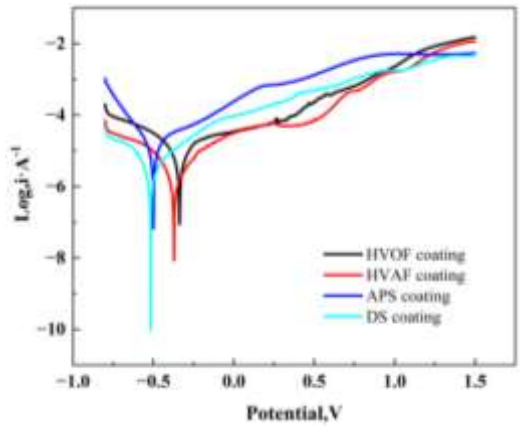

Fig. 8. Polarization curves of WC-10Co-4Cr coatings fabricated by different thermal spray technologies.

Extensive WC decomposition into W_2C occurred during air plasma spraying. As a result, abundant interlayer pores and unmelted particles existed in APS coating. Interfacial gaps, which have been formed between these defects and coating matrix, can act as channels for corrosive medium infiltration and induce internal intergranular and interfacial corrosion. And then the overall corrosion failure of the coating was accelerated [25]. It should be noted that the corrosion resistance of HVOF coating was superior to that of APS coating due to almost disappeared interparticle pores/microcracks and excellent cohesive strength. The corrosion resistance of HVAF coating was superior to that of the other three types of coatings owing to a denser microstructure. As reported by Vijaya Lakshmi et al. [26], the corrosive attack began with the (Co–Cr) binder phase leaching and formation of a pseudo-passive layer consisting of Co, Cr and/or W oxides on the surface of HVAF-sprayed WC-10Co-4Cr coatings during electrochemical corrosion tests. The interactions between corrosive media and the coating were inhibited and the protection effects were enhanced by this film. As reported by Shahbazi et al. [27], HVAF-sprayed HEA-based coatings exhibited 0.1 – 0.2 % porosity, versus 2.8 – 4.2 % for HVOF-sprayed MCrAlX coatings. And then corrosion resistance was directly improved due to higher density of HVAF coating. In addition, more superior corrosion resistance of HVAF coatings than that of DS ones was further confirmed by Alroy et al. [28].

Corroded morphologies of WC-10Co-4Cr coatings after immersion in NaCl solutions were presented as shown in Fig. 9. EDS analysis of the corresponding regions in corrosion surfaces can be found as shown in Table 3. Obvious corrosion pits and spallation traces were observed on the surface of the APS coating after immersion (Fig. 9 a). EDS analysis revealed that the oxygen content

in the corroded area of the APS coating reached as high as 62.32 at.%, while tungsten content decreased to 15.14 % (Table 3).

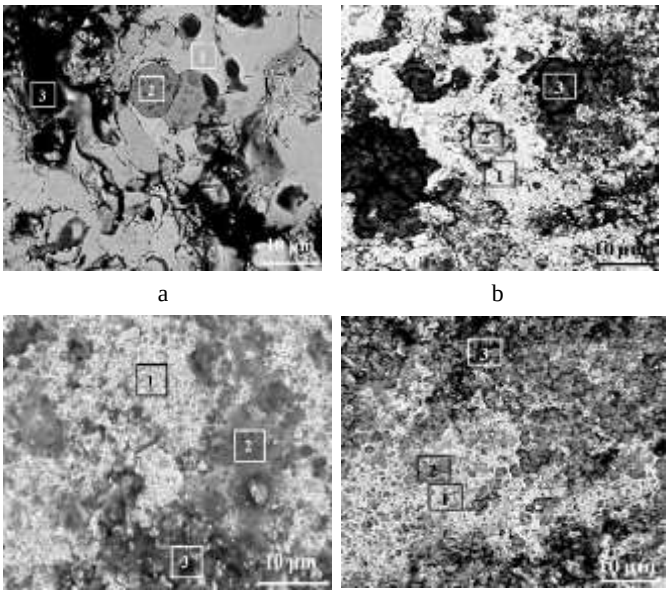

Fig. 9. SEM morphologies of WC-10Co-4Cr coatings prepared by: a – APS; b – DS; c – HVAF; d – HVOF after immersion in 3.5 wt.% NaCl solutions

Table 3. The corresponding EDS results indicated in Fig. 9

Sample	Point 1		Point 2		Point 3	
	W, at.%	O, at.%	W, at.%	O, at.%	W, at.%	O, at.%
APS coating	46.23	16.27	24.30	39.96	15.14	62.32
DS coating	37.41	14.80	25.32	21.11	12.59	62.97
HVOF coating	20.21	35.79	6.28	74.89	9.78	49.28
HVAF coating	30.18	18.65	18.57	56.53	13.56	45.18

Severe dissolution of WC phase occurred, and then a large amount of W_2C phase formed during APS. Electrochemical corrosion of APS coating was exacerbated owing to alteration of the corrosion microenvironment by W_2C phase. In addition, the inherent porous and striped defects of the APS coating further accelerated the penetration of corrosive media and then led to destruction of the coating structure. The failure mechanism was similar to the oxidative degradation of APS coatings induced by defects during thermal shock process [29, 30].

In contrast, the DS coating exhibited relatively slight corrosion damage after immersion, and only a small number of scattered corrosion spots with no obvious spallation can be found, as shown in Fig. 9 b. Oxygen contents of white (area 1), gray (area 2) and black (area 3) phases in the corroded area of DS coating increased from 14.80 to 21.11 and 62.97 at.% as shown in Table 3. The oxygen-rich regions corresponded to the zones where corrosion products and oxides/hydroxides preferentially formed in special regions such as W_2C phase and Co–Cr one, micropores and microcracks. The dense structure of DS coating hindered the intrusion of corrosive media. In addition, an inner Cr_2O_3 layer and an outer Co-based oxide/hydroxide layer were formed on surface of Fe-based metallic glass during electrochemical reactions [31]. And then further corrosion of DS coating was inhibited by this passive film due to fewer defects and higher chemical stability, which was consistent with the corrosion mechanism of HEA [32] and Fe-based amorphous coatings [33].

Similarly, the HVAF coating maintained the flattest surface after immersion, with only extremely slight corrosion traces and no obvious pits as shown in Fig. 9(c). Almost no decomposition of WC phase occurred during HVAF spraying. Co and Cr elements formed a continuous passive film on the surface of HVAF coating during electrochemical corrosion. As a result, the stability of the WC phase was confirmed owing to the protective effect of the passive film. The HVOF coating exhibited a small number of fine corrosion pits on the corroded surface, as shown in Fig. 9 d. The corrosion degree of the HVOF coating is between those of the DS and APS ones. This may be related to the partial decomposition of the WC phase and the presence of a small amount of interlaminar pores during the HVOF spraying process.

The corrosion mechanism of the WC-10Co-4Cr coating was mainly galvanic corrosion, which was exacerbated by the formation of interlaminar pores and W_2C phase. The WC phase in cemented carbide coating acted as the cathodic phase, while the Co-Cr binding phase served as the anodic phase, and microcells were formed during the corrosion experiment. As a result, the Co-Cr phase dissolved preferentially and Co^{2+} and Cr^{3+} ions were released simultaneously. Dense passive films such as Cr_2O_3 and CoO were formed on the corroded surface. The penetration and chemical attack of corrosive media can be effectively blocked by a passive film. However, the passive film was prone to rupture, which was further confirmed by corrosion pits, spallation traces and microdefects as shown in Fig. 9, owing to the formation of defects such as pores and cracks during thermal spraying. Corrosive media then penetrated through these defects, accelerating the dissolution of the Co-Cr phase and ultimately leading to coating corrosion failure.

4. CONCLUSIONS

1. WC-10Co-4Cr hard alloy coatings were prepared on the surface of 304 stainless steel substrate by APS, DS, HVOFS, and HVAFS, respectively. A typical lamellar structure can be found in APS coating. A large amount of the WC hard phase of APS coating decomposed during preparation. Initial particle structure of the feedstock was retained in DS, HVOF and HVAF coatings. Furthermore, the initial phase composition of the feedstock was still retained both in HVOF and HVAF coatings. The Vickers hardness of APS, DS, HVOF and HVAF coatings, which are much higher than that of 304 stainless steel substrate, are 771.4 HV, 954.2 HV, 1166.2 HV and 1162.2 HV, respectively.
2. The volume wear rates of APS, DS, HVOFS, and HVAFS coatings, which decreased sequentially, were $(7.93\pm0.30)\times10^{-5}$, $(1.51\pm0.20)\times10^{-5}$, $(1.17\pm0.10)\times10^{-5}$, and $(1.10\pm0.10)\times10^{-5}$ $mm^3/N\cdot m$, respectively. And they are all significantly lower than that of 304 stainless steel substrate (approximately

$(36.82\pm0.80)\times10^{-5}$ $mm^3/N\cdot m$). The average friction coefficients of 304 stainless steel substrate, APS coating, DS coating, HVOF coating, and HVAF coating, which also decreased sequentially, were (0.68±0.03), (0.56±0.02), (0.48±0.01), (0.44±0.01) and (0.43±0.01), respectively. The main wear mechanisms are abrasive wear and fatigue wear. The wear resistances of HVOF and HVAF coatings were superior to those of APS and DS ones. And the wear resistances of all thermal sprayed coatings were significantly higher than that of 304 stainless steel substrate.

3. E_{corr}, I_{corr} and R of APS coating in NaCl solution were approximately (-0.50±0.02) V_{SCE}, (19.97±0.06) $\mu A/cm^2$ and 1367.7 Ω, respectively. Those of DS coating were (-0.52±0.02) V_{SCE}, (3.12±0.03) $\mu A/cm^2$ and 13051.3 Ω, respectively. Compared to DS coating, the HVOF one had a higher I_{corr} of (7.74±0.04) $\mu A/cm^2$ and lower R of 5810.9 Ω. And then the corrosion resistance of the HVOF coating was slightly inferior to that of the DS one. The HVAF coating had the highest E_{corr} (-0.37±0.01) V_{SCE} and R (20438.5 Ω), the lowest I_{corr} (1.75±0.02 $\mu A/cm^2$). The order of corrosion resistance from high to low was HVAF coating, DS one, HVOF one and APS one, respectively. The corrosion performances of these four coatings were determined by their microstructures and phase compositions.

Acknowledgments

The authors would like to thank Mr. M.H. Yang and Z. Xie, Mrs. S.Y. Yang and J.Y. Hu, Hunan MAG New Material Technology Co. Ltd, for their assistance in providing characterization services to this study. This work was supported by Natural Science Foundation of Hunan Province of China (Grant No. 2025JJ50287), Key Research and Development Program of Hunan Province of China (2022GK2030).

REFERENCES

1. **Meng, Y., Li, X.W., Cheng, H.R.** Study on Wear Resistance of WC-10Co-4Cr Coatings Prepared by Different Thermal Spraying Technologies *Rare Metals and Cemented Carbides* 43 2015: pp. 25 – 28.
2. **Wang, Y.M., Xie, L., Wu, X.L., Li, C.L., Zhou, P.** Microstructure and Tribological Properties of FeCoCrNi High-Entropy Alloy Coatings Fabricated by Atmospheric Plasma Spraying *Journal of Materials and Engineering Performance* 32 2023: pp. 3475 – 3486. https://doi.org/10.1007/s11665-022-07331-0
3. **Wang, Y.M., Zhang, W., Chen, D.Q., Liu, X.B., Hu, W., Liu, L.F., Yan, J.H., Xiong, X.** High Temperature Friction and Wear Performance of TiB_2-50Ni Composite Coating Sprayed by HVOF Technique *Surface and Coatings Technology* 407 2021: pp. 126766. https://doi.org/10.1016/j.surfcoat.2020.126766
4. **Bolelli, G., Berger, L.M., Börner, T., Koivuluoto, H., Lusvarghi, L., Lyphout, C., Markocsan, N., Matikainen, V., Nylén, P., Sassatelli, P., Trache, R., Vuoristo, P.** Tribology of HVOF- and HVAF-Sprayed WC-10Co4Cr Hardmetal Coatings: A Comparative Assessment *Surface and Coatings Technology* 265 2015: pp. 125 – 144. https://doi.org/10.1016/j.surfcoat.2015.01.048
5. **Xie, L., Xiong, X., Zeng, Y., Wang, Y.M.** The Wear Properties and Mechanism of Detonation Sprayed Iron-Based Amorphous Coating *Surface and Coatings Technology* 366 2019: pp. 146 – 155. https://doi.org/10.1016/j.surfcoat.2019.03.028
6. **Yuan, B., Yuan, X.J., Zha, B.L., Chen, X.H., Yu, Z.H., Li, Z.L.** Corrosive-Tribological Behavior and Decarburization Mechanism of WC-10Co4Cr Coatings Deposited by Plasma Spraying *Hot Working Technology* 46 2017: pp. 159 – 163.
7. **Yuan, X.J., Zha, B.L., Chen, X.H., Yu, Z.H., Wang, X.J., Yang, N.J., Yao, C.J.** Microstructure Evolution and Corrosion Wear Resistance of Plasma Spraying WC-10Co-4Cr Coatings *Rare Metal Materials and Engineering* 48 2019: pp. 473 – 481.
8. **Huang, B., Wu, Q.D., Wei, X.L., Xiao, J.K., Zhang, G., Zhang, C.** Tribocorrosion Behaviors of High Velocity Oxygen-fuel Sprayed WC-10Co-4Cr Coatings *Surface Technology* 49 2020: pp. 285 – 293.
9. **Yang, W.H., Wu, Y.P., Hong, S., Li, J.H., Li, B.T.** Microstructure, Friction and Wear Properties of HVOF Sprayed WC-10Co-4Cr Coating *Journal of Materials Engineering* 46 2018: pp. 120 – 125. https://doi.org/10.11868/j.issn.1001-4381.2016.000770
10. **Murthy, J.K.N., Venkataraman, B.** Abrasive Wear Behaviour of WC–CoCr and Cr_3C_2-20(NiCr) Deposited by HVOF and Detonation Spray Processes *Surface and Coatings Technology* 200 2006: pp. 2642 – 2652. https://doi.org/10.1016/j.surfcoat.2004.10.136
11. **Murthy, J.K.N., Rao, D.S., Venkataraman, B.** Effect of Grinding on the Erosion Behaviour of a WC–Co–Cr Coating Deposited by HVOF and Detonation Gun Spray Processes *Wear* 249 2001: pp. 592 – 600. https://doi.org/10.1016/S0043-1648(01)00682-2
12. **Thakare, M.R., Wharton, J.A., Wood, R.J.K., Menger, C.** Exposure Effects of Strong Alkaline Conditions on the Microscale Abrasion–corrosion of D-gun Sprayed WC-10Co-4Cr Coating *Tribology International* 41 2008: pp. 629 – 639. https://doi.org/10.1016/j.triboint.2007.07.012
13. **Samodurova, M., Shaburova, N., Samoilova, O., Moghaddam, A.O., Pashkeev, K., Ul'yanitckiy, V., Trofimov, E.** Properties of WC-10%Co-4%Cr Detonation Spray Coating Deposited on the Al-4%Cu-1%Mg Alloy *Materials* 14 2021: pp. 1206. https://doi.org/10.3390/ma14051206
14. **Huang, W., Zhang, J.P., Wang, W., Li, D.J., Wang, B.** Study on Blasting Erosion Performance of WC-10Co-4Cr Coating Sprayed by HVAF *Thermal Spray Technology* 14 2022: pp. 35 – 44.
15. **Lian, Y., Li, Y., Wang, J.M., Wu, H.** Erosion Resistance of HVOF/AC-HVAF Sprayed WC-10Co-4Cr Coatings *Transactions of the China Welding Institution* 40 2019: pp. 95 – 100.
16. **Wu, Y.M., Chen, X.M., Zhou, X.L., Wang, L.R., Zhao, J., Fu, L., Mao, P.Z.** Properties and Wear Mechanism of WC-10Co-4Cr Coatings Prepared by SPS and HVOF *Transactions of Materials and Heat Treatmen*t 37 2016: pp. 165 – 171.
17. **Picas J.A., Rupérez, E., Punset, M., Forn, A.** Influence of HVOF Spraying Parameters on the Corrosion Resistance of

WC-CoCr Coatings in Strong Acidic Environment *Surface and Coatings Technology* 255 2013: pp. 47 – 57. https://doi.org/10.1016/j.surfcoat.2013.03.015

18. **Cheng, Y., Yi, H., Yang, J., Cao, H., Li, R.** Ultrasonic Vibration-assisted Cored Wire Arc Additive Manufacturing of WC-reinforced 316 L Composite Coatings: Microstructure and Wear Performance *Surface and Coatings Technology* 522 2026: pp. 133185. https://doi.org/10.1016/j.surfcoat.2026.133185
19. **Jia, L., Yi, H., Cao, H., Luo, J.** Laser Shock Peening of TiC/Inconel 625 Composites Fabricated Via Cored Wire Arc Additive Manufacturing *Journal of Materials Processing Technology* 348 2025: pp. 119190. https://doi.org/10.1016/j.jmatprotec.2025.119190
20. **Jia, L., Yi, H., Jiao, F., Cao, H.** Particle Floating and Transfer Effect in Cored Wire Arc Additive Manufacturing: Formation Mechanism and Laser Shock Inhibition *International Journal of Machine Tools and Manufacture* 207 2025: pp. 104260. https://doi.org/10.1016/j.ijmachtools.2025.104260
21. **Yuan, X.J., Zha, B.L., Chen, X.H., Yu, Z.H., Wang, X.J.** Corrosion Resistance of WC-10Co-4Cr Coatings in NaCl and Acid Solution at Different Temperatures *Journal of Materials Engineering* 47 2019: pp. 63 – 71. https://doi.org/10.11868/j.issn.1001-4381.2017.001551
22. **Guilemany, J.M., Nutting, J., Sobolev, V.V., Dong, Z., Paco, J.M., de Calero, J.A., Fernandez, J.** Interface Structures of High Velocity Oxy-fuel Sprayed WC-Co Coating on a Copper Substrate *Materials Science & Engineering A* 232 1997: pp. 119 – 128. https://doi.org/10.1016/S0921-5093(97)00108-1
23. **Dent, A.H., Depalo, S., Sampath, S.** Examination of the Wear Properties of HVOF Sprayed Nanostructured and Conventional WC-Co Cermets with Different Binder Phase Contents *Journal of Thermal Spray Technology* 11 2016: pp. 551 – 558. https://doi.org/10.1361/105996302770348691
24. **Hou, G.L., An, Y.L., Liu, G., Zhou, H.D., Chen, J.M., Chen, Z.J.** Effect of Atmospheric Plasma Spraying Power on Microstructure and Properties of WC-$(W,Cr)_2C$-Ni Coatings *Journal of Thermal Spray Technology* 20 2011: pp. 1150 – 1160. https://doi.org/10.1007/s11666-011-9661-x
25. **Yang, K., Jiang, Z., Chen, C., Zhang, S., Liu, X.** Investigation on the Microstructure, Tribological Performance and Corrosion Resistance of Ni-Mo Coatings Deposited by HVOF and APS Methods *Vacuum* 200 2022: pp. 111023. https://doi.org/10.1016/j.vacuum.2022.111023
26. **Vijaya Lakshmi, D., Suresh Babu, P., Wasekar Nitin, P., Sivakumar, G., Prasad, M.J.N.V.** Electrochemical Corrosion Behavior of Thin and Thick WC-10Co-4Cr Coatings Deposited by HVAF Thermal Spray Technique *Surface and Coatings Technology* 511 2025: pp. 132318. https://doi.org/10.1016/j.surfcoat.2025.132318
27. **Shahbazi, H., Lima, R.S., Stoyanov, P., Moreau, C.** Enhanced Oxidation Resistance of High-entropy Alloy Bond Coats via Low-temperature Spray Processing and Vacuum Heat Treatment *Surface and Coatings Technology* 515 2025: pp. 132655. https://doi.org/10.1016/j.surfcoat.2025.132655
28. **Alroy, R.J., Kamaraj, M., Lakshmi, D.V., Praveen, K., Babu, P.S., Sivakumar, G.** Tailoring Microstructural Features of Cr_3C_2-25NiCr Coatings through Diverse Spray Variants and Understanding the High-temperature Erosion Behavior *Tribology International* 188 2023: pp. 108810. https://doi.org/10.1016/j.triboint.2023.108810
29. **Huang, J.B., Sun, W., Huang, R.Z., Ma, W.H.** Cracking Behavior of Atmospheric Plasma-sprayed 8YSZ Thermal Barrier Coatings during Thermal Shock Test *Coatings* 13 2023: pp. 243. https://doi.org/10.3390/coatings13020243
30. **Wang, Y., Tian, W., Yang, Y.** Thermal shock Behavior of Nanostructured and Conventional Al_2O_3/13wt%TiO_2 Coatings Fabricated by Plasma Spraying *Surface and Coatings Technology* 201 2007: pp. 7746 – 7754. https://doi.org/10.1016/j.surfcoat.2007.03.015
31. **Hua, N.B., Hong, X.S., Liao, Z.L., Zhang, L., Ye, X.Y., Wang, Q.T., Liaw, P.K.** Corrosive Wear Behaviors and Mechanisms of a Biocompatible Fe-based Bulk Metallic Glass *Journal of Non-Crystalline Solids* 542 2020: pp. 120088. https://doi.org/10.1016/j.jnoncrysol.2020.120088
32. **Wen, X., Cui, X.F., Jin, G., Liu, Y.F., Zhang, Y., Zhang, X.R., Liu, E.B., Tian, H.L., Fang, Y.C.** Corrosion and Tribo-corrosion Behaviors of Nano-lamellar Ni1.5CrCoFe0.5Mo0.1Nbx Eutectic High-entropy Alloy Coatings: the Role of Dual-phase Microstructure *Corrosion Science* 201 2022: pp. 110305. https://doi.org/10.1016/j.corsci.2022.110305
33. **Cui, S., Zhai, H.M., Tong, W., Li, W.S., Li, X.Q., Fan, X.J., Xiong, D.S.** Corrosion and Tribo-corrosion Behaviors of Detonation Sprayed Fe-based Amorphous Coating *Surface and Coatings Technology* 482 2024: pp. 130717. https://doi.org/10.1016/j.surfcoat.2024.130717